Int. J. Heat Mass Transfer, Accepted Version, 2018
DOI: 10.1016/j.ijheatmasstransfer.2017.12.148

Saturated pool boiling enhancement using porous lattice structures produced by Selective Laser Melting

K.K. Wong, K.C. Leong*
Singapore Centre for 3D Printing, School of Mechanical and Aerospace Engineering, Nanyang Technological University, 50 *Nanyang Avenue, Singapore* 639798, *Republic of Singapore*

ABSTRACT

Pool boiling heat transfer of saturated FC-72 under atmospheric pressure was studied for porous lattice structures fabricated using the Selective Laser Melting (SLM) technique. The substrates possess repeating geometry of octet-truss unit cell and were varied with unit cell sizes of 2.0 mm, 3.0 mm and 5.0 mm and structure heights of 2.5 mm, 5.0 mm and 10.0 mm. In comparison with a plain surface, the porous structures show significant enhancement in nucleate boiling heat transfer coefficients and delay of Critical Heat Flux (CHF). The enhancement is attributed to the increased surface area, increased nucleation site density and capillary-assisted suction of the porous structure. The porous structure allows sustained liquid replenishment which delayed the hydrodynamic choking and CHF significantly. The best performing substrate with the 3-mm unit cell size and 5-mm structure height has an average nucleate boiling heat transfer coefficient of 1.35 W/cm^2·K, which is 2.81 times that of the plain surface at 0.48 W/cm^2·K. Heat transfer mechanisms are proposed for the different heat flux levels of the porous structures based on visual observations. The boiling patterns are classified as low, mid, high and very-high heat flux levels. At high heat flux level, two separate modes of stable and unstable boiling patterns are observed. For the stable boiling pattern, there are distinct bubble departure and liquid replenishment pathways, thus allowing a good convection flow. However, for the unstable boiling pattern, there is major liquid-vapor counter-flow, which disrupts the orderly liquid replenishment pathway.

KEYWORDS: Nucleate pool boiling; porous media; 3D printing; Selective Laser Melting; FC-72

1. Introduction

Thermal management is of crucial importance to the advancement of the electronic industry due to the exponential increase in heat flux over the past decades. Conventional natural and forced convection cooling methods of single-phase fluid are not capable of removing the resulting high heat fluxes for maintaining an acceptable operational temperature. Pool boiling, which is a phase change cooling method, is widely applied to cool high power electronic equipment by researchers over the past decades. Dielectric liquids such as FC-72 and HFE-7000 were often used in pool boiling studies due to the electrical and chemical compatibility with electronic parts.

Extensive research efforts have been conducted to enhance the nucleate pool boiling heat transfer coefficient using surface modification techniques and porous media in the last decades. At high heat fluxes, a phenomenon known as the Critical Heat Flux (CHF) occurs when the vapor forms a film at the heated surface and impedes fluid replenishment. The vapor film introduces a high thermal resistance which usually results in a large increase in the surface temperature. Thus, CHF is typically the upper limit for pool boiling systems and researchers have attempted to delay the onset of CHF with enhanced surfaces.

1.1. Surface modification

A thorough literature review on the use of surface microstructures for pool boiling enhancement was performed by Honda and Wei [1]. Shojaeian and Koşar [2] and Kim et al. [3] compiled comprehensive reviews of pool and

* Corresponding author.
E-mail address: mkcleong@ntu.edu.sg (K.C. Leong)

DOI: 10.1016/j.ijheatmasstransfer.2017.12.148

Nomenclature

A	area (m^2)
C_p	liquid specific heat (J/kg·K)
D_p	average pore diameter (mm)
D_s	average strut diameter (mm)
h	heat transfer coefficient (W/cm^2·K)
q''	heat flux (W/cm^2)
k	thermal conductivity (W/m·K)
L	length (m)
p	pressure (Pa)
R	thermal resistance (K/m^2·W)
T	temperature (°C)

Greek Symbols

σ	surface tension (N/m)
ρ	density (kg/m^3)
θ	contact angle (°)
η	relative enhancement

Subscripts

al	aluminum
ave	average
cu	*copper*
ep	*epoxy*
sat	saturated
w	wall
ref	reference

flow boiling with micro- and nanostructured surfaces. More recently, Leong et al. [4] conducted a review of pool boiling heat transfer of dielectric fluids on enhanced surfaces.

For pool boiling, the total surface area and active nucleation sites play a major role to enhance heat transfer at the solid-liquid interface. Many researchers have applied fins with dimensions ranging from tens of micrometers to ten millimeters to enhance the boiling heat transfer. Wei and Honda [5] studied the effect of fin geometry on boiling heat transfer from silicon chips with micro-pin-fins immersed in FC-72. The silicon chip has a base area of 10 mm by 10 mm and the micro-pin-fin was produced by a dry etching technique. Significant enhancement in heat transfer coefficients and delay of CHF were reported using micro-pin-fins surfaces. Yu and Lu [6] performed pool boiling experiments on copper blocks with a base area of 10 mm by 10 mm in saturated FC-72. Finned surfaces with fin thickness varying from 0.5 mm to 2.0 mm and heights varying from 0.5 mm to 4.0 mm were compared to a plain copper block. The results showed that the finned surfaces improved heat transfer due to their larger surface areas. However, the heat transfer enhancement was not proportional to the total surface area increase due to the finned surfaces. It was also observed that coalescence of bubbles occurred more readily for substrates with fins of small gaps, resulting in longer lift-off times. Rainey and You [7] also studied pool boiling on copper blocks with finned surfaces of different heights of 1 - 8 mm. It was reported that heat transfer enhancement occurred for fin heights up to 5 mm and further increase in the height did not contribute to increasing nucleate boiling as the surface temperature of the upper portion of the fin was too low to sustain boiling.

Coated surfaces have also been explored to enhance pool boiling heat transfer. O'Neill et al. [8] proposed that the pores formed by inter-connected particles act as active nucleation sites, such that vapor is generated in the inter-particle space and squeezed out of the open pores. The escaped vapor is then refilled with liquid from adjacent pores that act as liquid supply channels. Cieśliński [9] produced metallic coatings using various methods of deposition such as electrolytic treatment, plasma spraying and gas-flame spraying on flat surfaces and external surfaces of stainless steel tubes. It was indicated that good metallic contact of the coatings and the substrate base was important for heat transfer. Webb [10] studied nucleate boiling from coatings of different parameters such as particle diameter, coating thickness and pore sizes. His results indicated that the maximum heat transfer coefficient was obtained for coating thickness of about three to four times the mean particle diameter for a highly conductive surface such as copper although it was not so for a less conductive material such as bronze. The pore size was suggested to produce a more significant effect as compared to particle size. Chang and You [11] coated diamond particles on a square heater. Pool boiling with saturated FC-72 yielded increased CHF from about 15 W/cm^2 to 28 W/cm^2 as compared with a plain surface. The porous surfaces also allowed reduction in boiling incipience superheat of about 80% to 90%, and 30% enhancement of heat transfer coefficients, as compared to plain surface. The enhancement was attributed to increased number of active

DOI: 10.1016/j.ijheatmasstransfer.2017.12.148

nucleation sites. Liter and Kaviany [12] developed a modulated porous surface of conical shapes with copper powder of 200 μm for pool boiling tests with pentane as working fluid under saturated conditions. It was suggested that in the porous layers, the liquid supply and vapor escape occurred as a liquid-vapor counter-flow which tended to resist the motions of each other. The liquid and vapor flow resistance increased as the heat flux increased, leading to choking of liquid replenishment and local dry-out, which caused CHF. Patil and Kandlikar [13] fabricated microporous coatings selectively on fin tops of open micro-channels on a 10 mm by 10 mm copper substrate. Pool boiling was tested with water at saturated conditions. The CHF was enhanced and a significant reduction in wall superheat was achieved as compared to a plain surface and a micro-channel surface with no microporous coatings. From high-speed visualization, it was observed that the bubbles nucleated from the top of the fins with microporous surface. It was proposed that the micro-channels acted as passages for water supply from all sides, creating a convective flow. Chemical vapor deposition has been investigated by Ho et al. [14] to coat carbon nanotubes on silicon surfaces for pool boiling study. In their investigation, the average heat transfer coefficient of coated surface showed improvement of up to 86% as compared to a plain surface. However, one drawback of this method is the tendency of the coating to degrade and peel off over time.

1.2. Porous foams

Recent developments in material processing technology have led to an emergence of lightweight porous foams for structural and thermal applications. According to the review on the thermal transport of metal foams by Zhao [15], these open-celled foams have high surface-to-volume ratio of 1000-3000 m^2/m^3. Additionally, heat transfer can be improved by enhanced fluid flow mixing due to the tortuosity of metal foams. The porous foams are typically classified under factors of material, porosity and pore density. The materials available are aluminum, steel and copper alloys. The porosity is determined by the volume fraction of void against bulk solid volume. The pore density is typically measured in pores per inch (PPI) by taking the average of the linear line pore density.

Some researchers have conducted measurements on the effective thermal conductivities of porous foams. Paek et al. [16] showed that the effective thermal conductivity increased as the porosity was decreased; however, when the porosity was fixed, no obvious change in effective thermal conductivity was detected when the cell size of the foam was varied. Due to the differences in material and pore geometry for different foams, theoretical modeling of thermal transport in porous foams is still very limited. Leong and Li [17] used a unit cell model to represent the pore structure of graphite foam in order to obtain the effective thermal conductivity. Their results showed that the effective thermal conductivity decreased with the increase of porosity. However, the fluid thermal conductivity was found to have negligible effect on the effective thermal conductivity.

Studies on pool boiling using porous foams were limited to commercially-produced foams. Xu et al. [18] conducted pool boiling experiments on copper foams using acetone as the fluid and studied the bubble characteristics using high-speed photography. The porosities of copper used were 0.88 and 0.95, while the pore densities were 30, 60 and 90 PPI. Pool boiling at low heat fluxes showed that miniature bubbles nucleated on the foam ligaments at specific locations. Increase of heat flux caused coalescence of the miniature bubbles into cage-shaped bubbles, which were larger than the pore diameter of the foam. Xu et al. [19] performed saturated pool boiling of deionized water on copper foams. Porosities of range 0.90-0.98, pore density of range 5-40 PPI and foam thickness of range 5-7 mm were used. It was postulated that the heat transfer surface area and bubble escape resistance were of significant importance in pool boiling heat transfer and these two factors compete with each other. Xu and Zhao [20] investigated the effect of cutting V-shaped grooves on copper foams for pool boiling experiments. It was shown that the V-shaped grooves reduced the bubble escape resistance and helped to delay CHF as compared to foams without grooves. For foams with smaller pores, the larger contact area between the escaping bubbles and metal struts caused stronger friction on the bubbles, thus, increasing the bubble resistance. However, smaller pores contribute to stronger capillary force of liquid flow and allowed better liquid replenishment. Hence, it was proposed that capillary force and bubble escape resistance are two contradictory forces for pool boiling of foams of small pores and high pore densities. Xu and Zhao [21] subsequently investigated pool boiling of gradient foams. Two foams of different pore densities were sintered together to form a single foam. By using a foam of higher pore density at the lower part, and another foam of

DOI: 10.1016/j.ijheatmasstransfer.2017.12.148

lower pore density at the upper part, we can achieve improved nucleation due to larger surface area at the base, and lower bubble escape at the upper portion. Pool boiling investigations on graphite foams have been investigated by Jin et al. [22] and Pranoto et al. [23]. In both cases, the graphite foams have shown significant nucleate boiling heat transfer enhancements as compared to a plain copper surface. The high ligament thermal conductivity of graphite has allowed the foam to maintain a high effective thermal conductivity and allowed good nucleation.

1.3. Selective Laser Melting

Selective Laser Melting (SLM) is an additive manufacturing technique, which is commonly known as 3D printing. It allows fabrication of metallic substrates from a powder base using a high-power laser source in a layer-by-layer fashion [24]. A three-dimensional geometry can be modeled using Computer-Aided Design (CAD) software and subsequently input into the SLM machine. The main advantages of SLM are the ease of fabrication of complex geometries and the near-net shape of the built parts which eliminates the need for a mold or long post-processing methods often required in casting [25].

In the recent years, the SLM technique has been explored to produce customized devices for heat transfer applications. The use of aluminum alloys such as AlSi10Mg and Al6061 allows fabrication of products which have high thermal conductivity. Wong et al. [26] produced five heat sinks of various fin geometries using Al6061 material for air convective heat transfer and reported heat transfer enhancement for fins of elliptical and V-shaped geometries. In other air convective heat transfer studies, Wong et al. [27] and Ho et al. [28] produced heat sinks consisting of fins of airfoil cross-sections using AlSi10Mg material. By comparing to the fins of cylindrical geometry, the airfoil fins showed superior heat transfer performance and lower pressure drop due to their streamline geometry. Neugebauer et al. [29] fabricated a miniature water cooler unit using AlSi10Mg material and showcased that the process of SLM allowed a better design approach to improving efficiency as delicate and complex geometries were buildable. Ho and Leong [30] investigated the use of porous inserts to enhance the thermal and hydraulic performance of water-cooled cold plates using SLM of AlSi10Mg material. Heat transfer enhancement of up to 383% as compared to an empty channel was obtained. Despite the above-mentioned studies of employing SLM to enhance single-phase heat transfer, there is limited literature on the use of SLM to fabricate structures for two-phase studies. Recently, Ho et al. [31] employed SLM to investigate pool boiling enhancements using surfaces of micro-fin and micro-cavity geometries. Using FC-72 as the fluid at atmospheric condition, the substrates achieved up to 70% improvement in heat transfer coefficient and 76% enhancement in CHF as compared to a plain surface. Esarte et al. [32] demonstrated heat pipe wick manufacturing using the SLM technique and conducted a study of the optimized wick design for a two-phase cooling system. The above literature review showcases the potential of using SLM as a manufacturing technique for heat transfer enhancement studies.

1.4. Aims of study

In this paper, the authors aim to study the pool boiling performance of porous lattice structures fabricated using the SLM technique. Compared to commercial metallic foams which tend to have limited pore structure design, random pore size distribution and inter-connectivity issues, SLM can produce intricate and complex porous lattice structures with highly controllable repeating unit cells. This would allow the geometrical effects of the porous structures on boiling heat transfer to be controlled more accurately. To the best of the authors' knowledge, there is no publication on pool boiling enhancement using porous lattice structures fabricated by SLM or other 3D printing techniques. Also, reported studies on pool boiling of porous structures using dielectric fluids are scarce. In this study, FC-72 was used as the working fluid at saturated condition under atmospheric pressure. The pool boiling heat transfer performance and delaying of CHF will be studied using porous lattice structures by varying the structure heights and unit cell sizes. Pool boiling mechanisms are also proposed based on a visualization study of the boiling process for different ranges of heat fluxes.

2. Substrate preparation and characterization

2.1 Selective Laser Melting process

DOI: 10.1016/j.ijheatmasstransfer.2017.12.148

The SLM 250 HL (SLM Solutions GmbH) facility was employed for the fabrication of substrates in the present study. It is housed in the Future of Manufacturing Laboratory 1 under the Singapore Centre for 3D Printing (SC3DP) at Nanyang Technological University (NTU), Singapore. A Gaussian distributed Yb:YAG laser of maximum power of 400 W and laser beam spot size of 80 μm was used for melting the metal powder. During operation, the build chamber was flushed with inert argon gas to attain an oxygen level of less than 0.2 % to minimize oxidation and combustion of powder.

During the manufacturing process, the powder was first distributed evenly on a substrate base plate. The laser scanning melted the powder according to a pre-programmed pathway that was defined in CAD file. The powder layer was rapidly melted and then solidified to form a thin solid layer. The powder bed was then lowered by one layer and redeposited. Laser scanning subsequently melted and bonded the new layer to the previous layer. This process was repeated until the entire part was formed.

In this study, the material used was AlSi10Mg due to the high thermal conductivity of up to 170 W/m·K for as-built products. The composition of the AlSi10Mg powder, as provided by the supplier, is listed in Table 1. Spherical powder with a distribution size of 20 μm to 63 μm was used. A Scanning Electron Microscope (SEM) image of the powder at a magnification of 300 times is shown in Fig. 1. In the current SLM process, the laser power, scanning speed, hatching spacing and layer thickness were selected to be 350 W, 1150 mm/s, 0.17 mm and 0.050 mm, respectively. These parameters were shown to produce substrates of high relative density from a previous study by Sing et al. [33] for the AlSi10Mg material. Three cubes of 1 cm^3 volume were fabricated using the above-mentioned parameters and their relative densities were evaluated using Archimedes' principle on a XSE204 Analytical Balance (Mettler-Toledo) machine. A high relative density of average 99.1% was obtained and the current parameters were demonstrated to be suitable for processing of AlSi10Mg powder.

Table 1. Percentage composition of AlSi10Mg alloy used

Al	Si	Fe	Cu	Mn	Mg	Ni	Zn	Pb	Sn	Ti
Balance	9.0-11.0	0.55 max	0.05 max	0.45 max	0.2-0.45	0.05 max	0.10 max	0.05 max	0.05 max	0.15 max

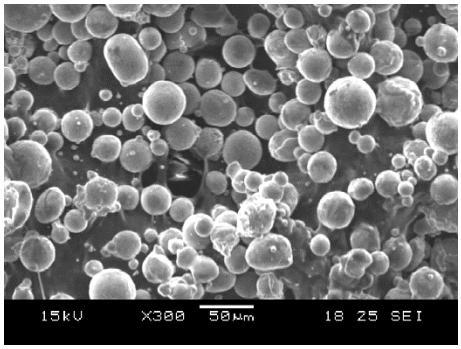

Fig. 1. SEM image of AlSi10Mg powder at a magnification of 300 times

2.2. Description of substrates

In this study, the octet-truss geometry was chosen as the repeating unit cell for the porous lattice structure. Fig. 2(a) shows a unit cell of the octet-truss lattice [34]. It consists of an octahedral cell in the center which is depicted in darkened shade, and eight tetrahedral cells at the edges. One example of the tetrahedral cell is shown with nodes labeled as p1 to p4. By repeating the unit cells in a 3D manner, an orderly porous lattice structure can be generated. Using the "Magics" software (Materialise), porous lattice structures of different unit cell sizes of 2 mm, 3 mm and 5 mm were created. The base area of the structure was fixed at 10 mm by 10 mm to be mounted onto the pool boiling facility, which would be described in the next section. For each unit cell size, three different structure heights of 2.5 mm, 5.0 mm and 10.0 mm were created. A total of nine porous lattice

DOI: 10.1016/j.ijheatmasstransfer.2017.12.148

structures were fabricated using SLM as the manufacturing process. For each substrate, the porous structure was built on a solid base of 1 mm thickness to allow easy mounting to the pool boiling facility. Examples of the fabricated porous structures at height of 10.0 mm with different unit cell sizes are shown in Fig. 2(b). A plain copper surface that was polished to a mirror-like finish was used as a benchmark for comparison. An abbreviation for naming the substrates is defined for easy reference in the subsequent portion of this paper. An example of the substrate with the name of Octet-2.0C-2.5H has a unit cell of 2.0 mm and structure height of 2.5 mm. A summary of the substrate parameters is shown in Table 2.

(a) (b)

Fig. 2. (a) Unit cell representation of the octet-truss lattice [34] (b) Fabricated substrates with 2-mm, 3-mm and 5-mm unit cells from left to right

Table 2. Summary of substrate characteristic

S/n	Name	Unit cell size (mm)	Height of structure (mm)
1	Plain surface	-	-
2	Octet-2.0C-2.5H	2	2.5
3	Octet-2.0C-5.0H	2	5.0
4	Octet-2.0C-10.0H	2	10.0
5	Octet-3.0C-2.5H	3	2.5
6	Octet-3.0C-5.0H	3	5.0
7	Octet-3.0C-10.0H	3	10.0
8	Octet-5.0C-2.5H	5	2.5
9	Octet-5.0C-5.0H	5	5.0
10	Octet-5.0C-10.0H	5	10.0

2.3. Light optical imaging of substrates

The characterization of the lattice structure was performed using a light optical microscope (Olympus SZX7) with its in-built measurement software. It can be observed that the fabricated porous lattice structures are of a very orderly repeating form and the octet-truss geometry was preserved for the different unit cell sizes. The porous lattice also shows good inter-connectivity, which would be important for fluid to permeate throughout the structure. A closer examination of the struts shows the presence of partially sintered powder, which is typical of the SLM process. The partially sintered powders are homogenously distributed, which would act as potential nucleation sites for bubble generation.

Fig. 3 shows examples of the microscope images for the 2-mm, 3-mm and 5-mm unit cell sizes. The struts were observed to be of cylindrical geometry. The pores were formed by the tetrahedral cells and are of equilateral triangle geometry. The pore diameter was assumed to be the length of one of the pore edges. A total of 25 to 30 measurements were taken to determine the average pore and strut diameters for each unit cell size. The linear pore density of each unit cell size, in terms of pore per inch (PPI) measurement, was also tabulated for easy comparison to other literature. The surface-area-to-volume ratio was obtained from the “Magics software” by dividing the total curve surface area of the struts to the bulk volume occupied by the lattice structure. Generally, the smaller unit cell size has more struts and hence, a larger surface area for a fixed volume. The surface roughness effect was not considered in this calculation. As the surface roughness is the same across the different unit cell sizes, it would not change the trend of surface-area-to-volume ratio if it were to be considered. The

DOI: 10.1016/j.ijheatmasstransfer.2017.12.148

porosity (ε) for the different unit cell sizes was fixed at a value of 0.7 when the substrates were generated using the software. A summary of the various measurements is given in Table 3.

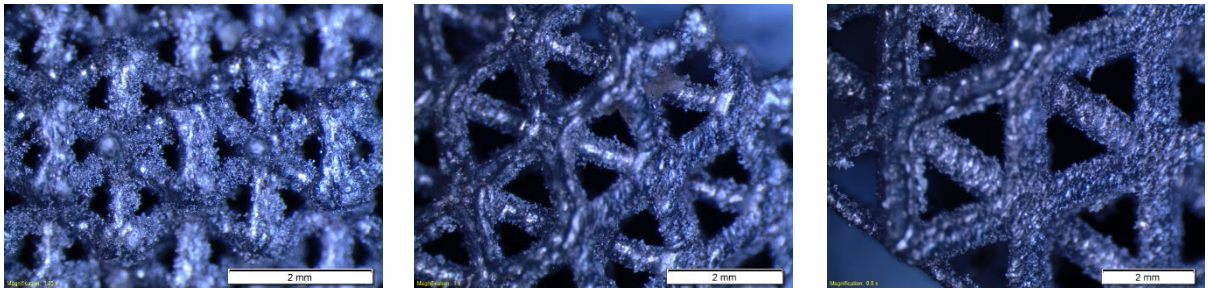

(a) (b) (c)

Fig. 3. Light optical microscope image of lattice of (a) 2-mm, (b) 3-mm unit and (c) 5-mm unit cell

Table 3. Substrate parameters for different unit cell sizes

Parameters	2-mm unit cell	3-mm unit cell	5-mm unit cell
Average pore diameter, D_p (mm)	0.53	1.03	1.72
Average strut diameter, D_s (mm)	0.31	0.48	0.85
Pore density (Pores per inch)	40	30	15
Surface-area-to-volume ratio (m^2/m^3)	2700	2200	1500

2.4. Topological mapping of substrates using confocal imaging

Surface roughness measurements were obtained using a PLμ Confocal Image Profiler on the struts of each unit cell size. Five random struts were chosen and 3D topographical mappings were obtained with step intervals of 1 μm. For each topographical mapping, six to eight linear profiles were further selected for linear surface roughness measurements. Fig. 4(a) shows a sample of the topological mapping of a strut on the 3-mm unit cell and Fig. 4(b) shows the distribution of surface roughness in terms of the root-mean-square (RMS) and average roughness (Ra) for each unit cell size. It can be concluded that the surface roughnesses are similar for the different substrates. This is because the surface roughness is mainly attributed to the partially sintered powder and rapid solidification process in SLM which is similar across all the substrates.

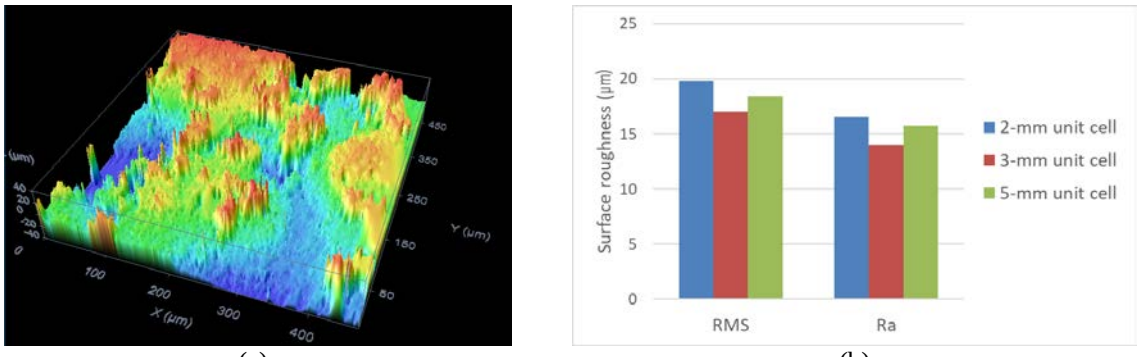

(a) (b)

Fig. 4. (a) Topological mapping of a strut on the 3-mm unit cell and (b) surface roughness distribution across different unit cell sizes

2.5. Wettability measurements of substrates

Surface contact angles were measured for a smooth copper surface using deionized water and FC-72. The surface contact angles were determined to be 93° for deionized water and 6° for FC-72 as illustrated in Fig. 5. This shows that FC-72 is a highly-wetting fluid which is beneficial for fluid replenishment into the porous lattice structure during the pool boiling process. As it is difficult to measure the surface contact angles for the porous lattice structure, the authors have adopted the method used by Ji et al. [35] in which the spreading time was used to characterize the surface wettability. A droplet of about 3 μL was gently deposited on the strut of the

DOI: 10.1016/j.ijheatmasstransfer.2017.12.148

lattice structure as shown in Fig. 6(a). Upon contact with the strut, the FC-72 droplet was quickly absorbed by the porous structure within 48 ms. Measurements of the different unit cell sizes yielded similar results of complete suction below 50 ms.

(a) Deionized water - 93° (b) FC-72 - 6°

Fig. 5. Contact angle measurement on smooth copper surface with (a) deionized water and (b) FC-72

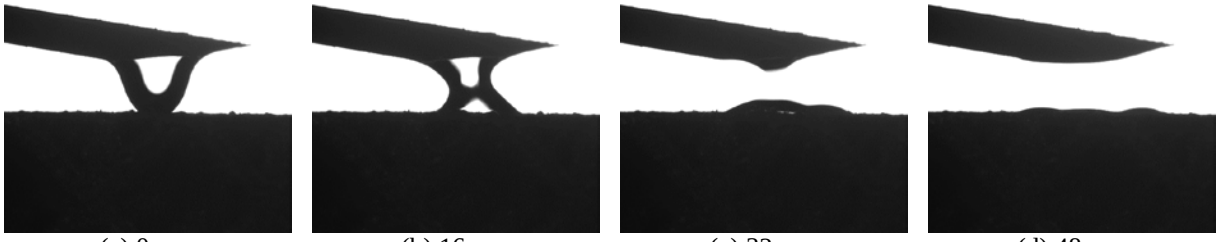

(a) 0 ms (b) 16 ms (c) 32 ms (d) 48 ms

Fig. 6. FC-72 droplet suction process for porous lattice structure

3. Pool boiling facility and data reduction

3.1 Pool boiling facility

A thermosyphon was used to investigate the saturated pool boiling of the substrates. The pool boiling facility used was similar to the one used by Ho et al. [31]. The schematic of the experimental setup is shown in Fig. 7. The pool boiling chamber with dimensions of 12 cm by 12 cm by 12 cm was constructed with an aluminum body and view glass panels to allow visualization of the boiling process. The base is supported by a Teflon block, while the top is covered with an aluminum plate of 2 cm thickness. The chamber was filled with dielectric fluid FC-72. Two cartridge heaters were submerged in the FC-72 to heat the fluid to its saturated temperature of 56°C, which was measured using two K-type thermocouples immersed in the fluid. A water-cooled condenser is situated above the fluid to recycle the condensed FC-72 back to the main pool during the boiling process. A refilling port at the top aluminum plate was left open to maintain the chamber at atmospheric pressure.

DOI: 10.1016/j.ijheatmasstransfer.2017.12.148

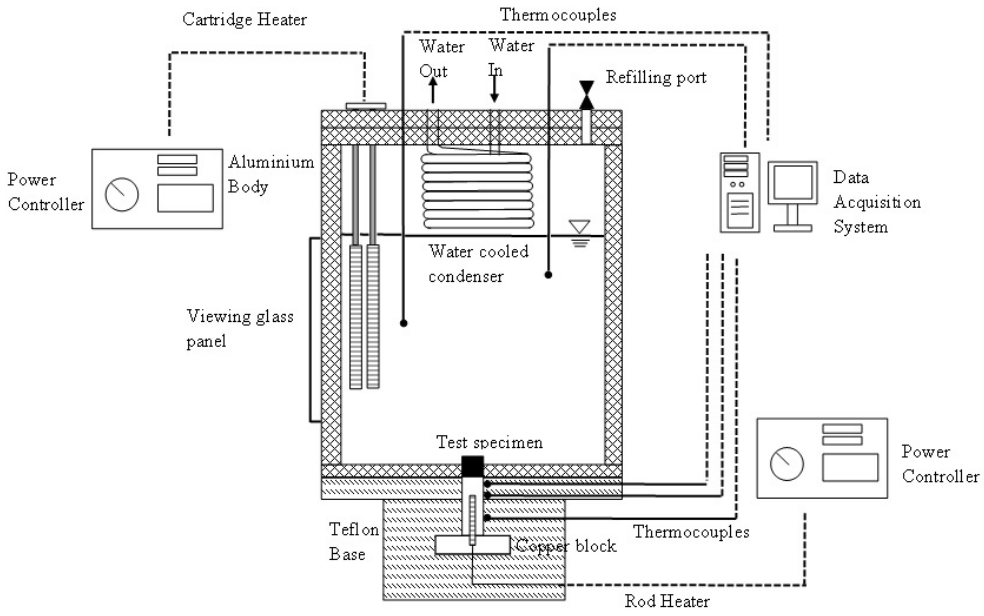

Fig. 7. Schematic of pool boiling facility [31]

A copper block was embedded in the center of the Teflon block. The test substrate was situated at the top of the copper block which has an exposed area of 10 mm by 10 mm. The test substrate was bonded to the top surface of the copper block using a thermal epoxy cement (Omegabond-200). A cylindrical heater of 6.24 mm diameter (Watlow Firerod) was embedded in the copper block to act as the heat-generating source. The power can be varied with a variable transformer, while the current and voltages can be measured accurately using in-built ammeter and voltmeter, respectively. The copper rod was thermally insulated at all sides using the Teflon base to allow heat to dissipate mainly through the top exposed surface. Three K-type thermocouples were positioned along the surface of the copper block through holes of 1 mm diameter drilled in the Teflon base, as shown in Fig. 8. The thermocouples T_1, T_2 and T_3 were placed at distances of 4 mm, 10 mm and 15 mm, respectively from the top surface of the substrate.

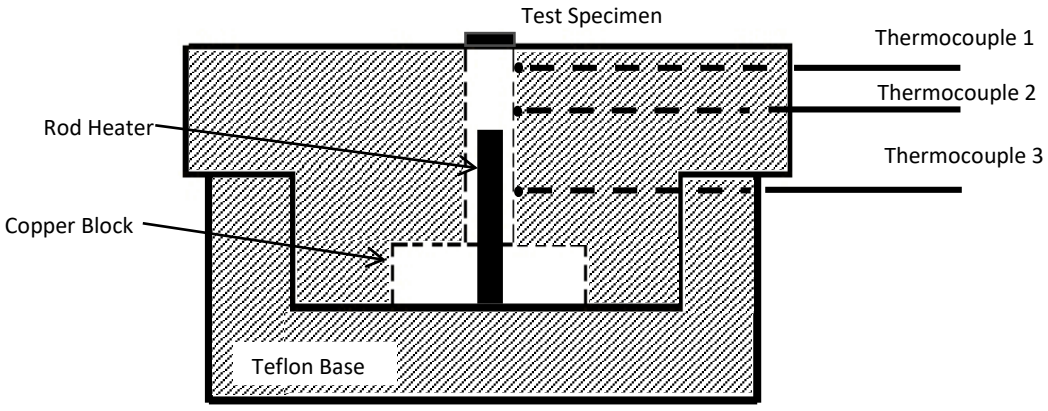

Fig. 8. Detailed drawing of Teflon base and thermocouple positions [31]

The total heat flux (q'') into the test substrates was calculated from temperatures of the top two thermocouples using Eq. (1), where k_{cu} is the thermal conductivity of copper, A is the cross-sectional area of the copper block and $L_{1\text{-}2}$ is the distance between Thermocouples 1 and 2. The total heat input to the rod heater was obtained from the product of the current and voltage input. The deviation of the electrical heat input and calculated heat transfer rate was attributed to heat loss, which accounted for about 5% of the total heat input.

DOI: 10.1016/j.ijheatmasstransfer.2017.12.148

$$q" = -k_{cu}\frac{T_1 - T_2}{L_{1-2}} \quad (1)$$

The wall temperature (T_w), which represents the temperature of the substrate top surface, was determined from the top-most thermocouple (T_1) using the thermal resistance model under one-dimensional steady-state conduction. The total resistance of the copper, epoxy and aluminum substrates is shown in Eq. (2). The thermal conductivities of the copper, epoxy and aluminum are assumed to be 400 W/m·K, 16 W/m·K and 170 W/m·K, respectively. Hence, the wall temperature (T_w) can be calculated using Eq. (3).

For the benchmark surface, the top of the copper block was used directly after polishing with grit 1200 sandpaper to a mirror-finish appearance. Hence, the thermal resistances of the epoxy and aluminum can be neglected from the modeling and only L_{cu} of 4 mm is considered from Thermocouple 1 to the top of the copper surface. For all porous structure substrates, the heights of combined copper block and porous structure substrates were measured using a Vernier caliper before and after applying the thermal epoxy. The thickness of the thermal epoxy (L_{ep}) is consistent at about 0.2 mm. For each substrate, the porous structure was built on a solid base of 1 mm thickness (L_{Al}) to allow easy mounting to the pool boiling facility.

$$R_{total} = R_{cu} + R_{ep} + R_{Al} = \frac{L_{cu}}{k_{cu}A} + \frac{L_{ep}}{k_{ep}A} + \frac{L_{Al}}{k_{Al}A} \quad (2)$$

$$T_w = T_1 - q"(R_{total}) \quad (3)$$

3.2. Properties of FC-72

In two-phase cooling systems, the thermophysical properties of the fluid used directly affect the heat transfer performance of the system. FC-72 from 3M Ltd was selected as the phase-change coolant due to its large dielectric strength and electrical non-conductivity. It is a dielectric fluid widely used for electronic cooling applications. FC-72 is also thermally and chemically stable, non-flammable, and practically non-toxic and have low Global Warming Potential. The thermophysical properties of FC-72 are summarized in Table 4 [36].

Table 4. Thermophysical properties of FC-72 at 1 atm [34]

Properties at saturation temperature (1 atm)	Value
Boiling point (°C)	56
Liquid density, ρ_l (kg/m^3)	1602.2
Vapor density, ρ_v (kg/m^3)	13.21
Liquid dynamic viscosity (kg/m·s)	4.33×10^{-4}
Liquid specific heat, C_p (J/kg·K)	1101
Liquid thermal conductivity, k (W/m·K)	0.054
Latent heat of vaporization (kJ/kg)	88
Liquid surface tension, σ (N/m)	7.83×10^{-3}
Dielectric strength at 0.1 inch gap (kV)	38

3.3 Experimental Procedures and Data Reduction

Experiments were conducted by first filling the pool boiling chamber with FC-72 such that the liquid level was approximately 60 mm above the test specimen. Electrical power was supplied to the two cartridge heaters in the bulk fluid to bring the fluid to saturation temperature (T_{sat}) of 56°C under atmospheric condition. To allow degassing of the bulk fluid, vigorous boiling was applied at saturated conditions for about 1 hour. Subsequently, the electrical power to the rod heater embedded in the copper block was raised at increments of between 1.0 and

DOI: 10.1016/j.ijheatmasstransfer.2017.12.148

5.0 W and the system could stabilize for between 20 to 50 minutes in the natural convection regime and 10 to 20 minutes in the nucleate boiling regime. For every increment, the steady-state condition was considered to be reached when the thermocouple reading was maintained within ± 0.5°C within a 2-minute period. The CHF condition was deemed to be reached when there was sudden huge temperature increase (approximately 5°C increase within 10 second) and bubble formation frequency was observed to decrease significantly. Thereafter, the power supply to the rod heater in the copper block was cut off to prevent overheating of the rod heater. For each test specimen, the experiment was carried out at least twice under similar conditions to ensure that the results were repeatable.

All thermocouples were calibrated prior to the experiments and the temperatures were acquired under quasi-steady-state condition with the Yokogawa MW100 data acquisition unit at the sampling rate of 2 Hz averaged over a duration of 1 minute. The saturation temperature of the bulk fluid was evaluated under atmospheric condition. Based on the measured $q"$, T_w and T_{sat}, the nucleate boiling heat transfer coefficient (h) was calculated from Eq. (4).

$$h = \frac{q"}{(T_w - T_{sat})} \tag{4}$$

The uncertainty of the K-type thermocouple measurements using was ± 0.2°C and the uncertainty of length measurements using a Vernier caliper was ±0.01 mm. Using the method described by Taylor [37], the average uncertainties of the heat transfer coefficient (h) and heat flux ($q"$) were determined from Eqs. (5) and (6). The uncertainty in h was higher in the low heat flux region as compared to higher heat fluxes, with a maximum of ± 20%. However, the uncertainty was estimated to be below ± 3.5% in the nucleate boiling regime above 15 W/cm^2.

$$\frac{\Delta h}{h} = \sqrt{\left(\frac{\Delta q"}{q"}\right)^2 + \left(\frac{\Delta T_w}{T_w - T_{sat}}\right)^2 + \left(\frac{\Delta T_{sat}}{T_w - T_{sat}}\right)^2} \tag{5}$$

$$\frac{\Delta q"}{q"} = \sqrt{\left(\frac{\Delta T_1}{T_1 - T_2}\right)^2 + \left(\frac{\Delta T_2}{T_1 - T_2}\right)^2 + \left(\frac{\Delta L_{1-2}}{L_{1-2}}\right)^2} \tag{6}$$

4. Results and discussions

4.1 Comparison of plain surface and porous structure

The saturated pool boiling curves of the plain surface and Octet-3.0C-2.5H are shown Fig. 9(a). The x-axis shows the surface superheat and the y-axis shows the heat flux. The corresponding heat transfer coefficients at different heat fluxes are shown in Fig. 9(b). For the plain copper surface, boiling incipience superheat was recorded at 12°C at the heat flux of 3 W/cm^2. However, for Octet-3.0C-2.5H, boiling incipience superheat was recorded at 2.6°C at 1 W/cm^2. The lower boiling incipience superheat and heat flux is due to the larger surface area and more active nucleation sites for the porous structure. The incipience nucleation is highly sensitive to the nucleation sites available on the surface. For the porous lattice structure, the rougher surface and intersections of struts form cavities which can be suitable for nucleation to occur readily, thus allowing lower boiling incipience superheat as compared to the plain surface.

The overall heat transfer performances (h_{ave}) of the substrates were calculated by averaging the heat transfer coefficients over the range of heat fluxes in the nucleate boiling regime. By using this computation method, the

DOI: 10.1016/j.ijheatmasstransfer.2017.12.148

h_{ave} values of the plain surface and Octet-3.0C-2.5H are 0.48 W/cm^2.K and 1.10 W/cm^2.K, respectively, showing an enhancement of 129% for the porous structure. For the plain surface, the CHF was 17.5 W/cm^2, whereas the CHF of Octet-3.0C-2.5H was 82 W/cm^2 corresponding to a delay of CHF by 369%.

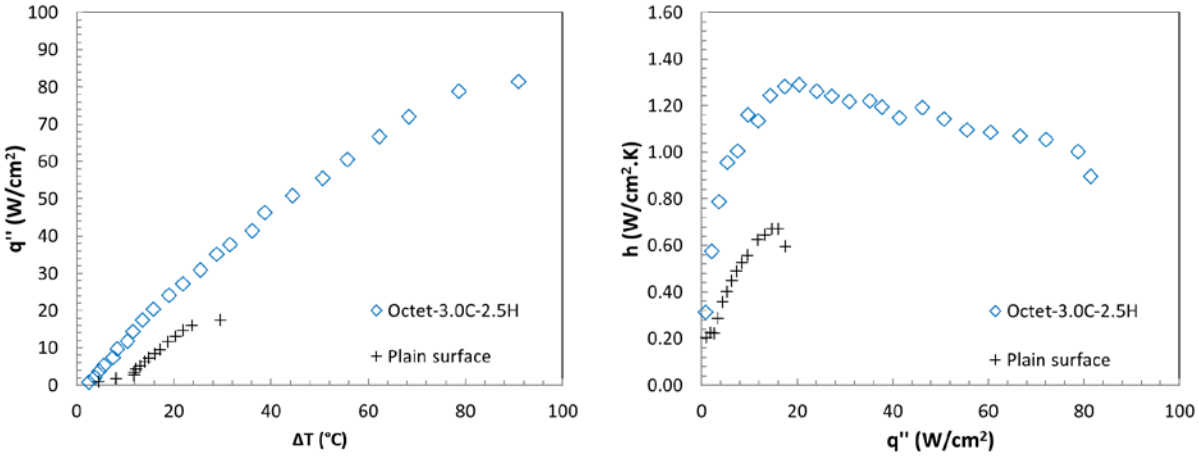

(a) (b)

Fig. 9. (a) Nucleate pool boiling curves and (b) heat transfer coefficients of plain copper surface and Octet-3.0C-2.5H

The macroscopic visualizations of pool boiling processes of the plain surface and Octet-3.0C-2.5H are depicted in Figs. 10 and 11, respectively. For the plain surface, individual nucleation of bubbles was observed at 5 W/cm^2 in Fig. 10(a). Coalescence occurred readily at 10 W/cm^2, forming mushroom-shaped bubbles as shown in Fig. 10(b). At 16 W/cm^2, a continuous vapor plume was observed as shown in Fig. 10(c). CHF was marked by a distinct vapor film or dry-out region forming at the base and corresponding reduction of bubble formation as shown in Fig. 10(d). The CHF occurred due to hydrodynamic instability as postulated by Zuber [38] and the liquid could not be replenished at the heated surface effectively, leading to a large increase in surface temperature. For the porous structure Octet-3.0C-2.5H, individual bubble nucleation occurred as shown in Fig. 11(a) at 7 W/cm^2. Coalescence of bubbles was delayed significantly as compared to plain surface. In Fig. 11(b), it can be observed that some coalescence occurred at 25 W/cm^2. In Fig. 11(c) at 58 W/cm^2, the bubble departure diameter increased and coalescence occurred rapidly to form a mushroom-shaped bubble encompassing the entire structure. Finally, CHF is deemed to occur at 82 W/cm^2 due to a sudden jump in superheat registered. As shown in Fig. 11(d), the bubble dynamics of porous structure is vastly different from the plain surface; the porous structure prevented the formation of vapor film and thus significantly delaying the CHF.

The enhancement of pool boiling of porous structure can be attributed to increased surface area, higher active nucleation site density and capillary-assisted suction. The solid struts of the porous structure act as conduction media for heat to spread upwards to the higher region of the structure. At higher heat flux, the temperature of the solid struts at the higher region can reach sufficiently high surface superheat to become active nucleation sites. The process of SLM typically causes partially sintered powder to be adhered to the surface of the structure. The surface roughness caused by the partially sintered powder can produce active nucleation sites for the boiling to occur.

Capillary-assisted suction allows liquid replenishment into the porous structure during the pool boiling process. The Young-Laplace equation for a capillary tube is shown in Eq. (7). Approximating the inter-connected pores as capillary tubes, it can be observed that a smaller pore diameter resulted in a larger capillary driving pressure, which should improve liquid replenishment. The estimated capillary pressures are 30 Pa, 15 Pa and 9 Pa for unit cell sizes of 2 mm, 3 mm and 5 mm, respectively. However, the liquid and vapor encounter form drag within the porous structure. A porous structure with smaller pore diameter results in a larger surface area which correspondingly increases the form drag, and thus reducing the effectiveness of bubble evacuation from the porous structure. The form drags of liquid and vapor are difficult to estimate as a deeper understanding of the effects of permeability and friction coefficients is required.

DOI: 10.1016/j.ijheatmasstransfer.2017.12.148

$$\Delta p = \frac{2\sigma cos\theta}{D_p} \tag{7}$$

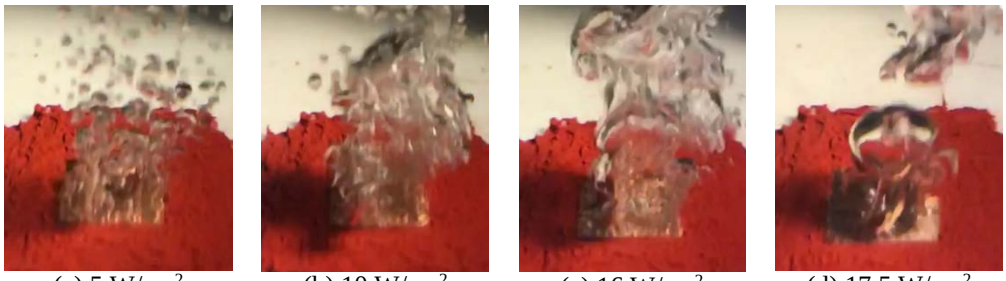

(a) 5 W/cm^2 (b) 10 W/cm^2 (c) 16 W/cm^2 (d) 17.5 W/cm^2 (CHF)

Fig. 10. Pool boiling visualization of plain copper surface at different heat fluxes

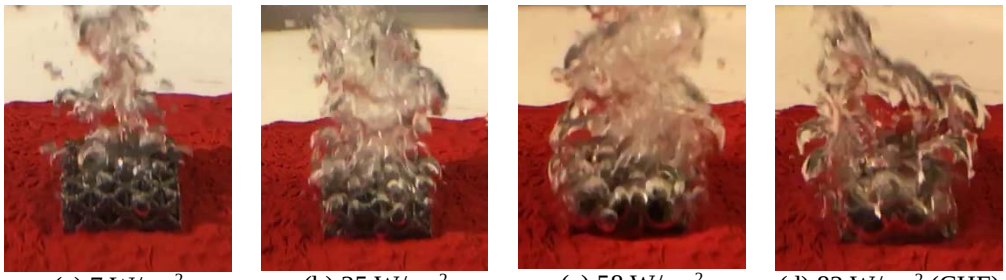

(a) 7 W/cm^2 (b) 25 W/cm^2 (c) 58 W/cm^2 (d) 82 W/cm^2 (CHF)

Fig. 11. Pool boiling visualization of Octet-3.0C-2.5H at different heat fluxes

4.2 Effect of unit cell size

Fig. 12(a) shows the pool boiling heat transfer performance of different unit cell sizes at a fixed structure height of 2.5 mm. The boiling curve of plain surface is also shown for comparison purpose. All the porous surfaces show enhancements in pool boiling performance as seen by the leftward shift of the curves as compared to the plain copper surface, i.e., a lower surface superheat is achieved at the same heat flux. The heat transfer performance increases with an increase in unit cell size. All the porous structures demonstrated delay of CHF as compared to the plain copper surface. The CHF for the 2-mm, 3-mm and 5-mm unit cell sizes were 71, 82 and 96 W/cm^2 respectively, showing an increasing trend with larger unit cell sizes. Fig. 12(b) shows the variation of heat transfer coefficient at the different heat fluxes for the same structures at height of 2.5 mm. It was observed that for heat fluxes below 10 W/cm^2, h is similar across the different structures. However, above 10 W/cm^2, the larger unit cell sizes performed better. The results show that for the structure height of 2.5 mm, bubble evacuation resistance is the dominant factor which affects nucleate boiling. The larger pore diameter allows less resistance and more rapid bubble evacuation, thus allowing high rate of heat transfer and delayed CHF. Fig. 13 shows the boiling patterns of the three substrates with 2.5 mm structure height size at a heat flux of 40 W/cm^2. The boiling process is vigorous and the bubbles encompassed the entire substrates. It can be observed that the 5-mm unit cell size exhibits relatively larger bubble size at departure.

DOI: 10.1016/j.ijheatmasstransfer.2017.12.148

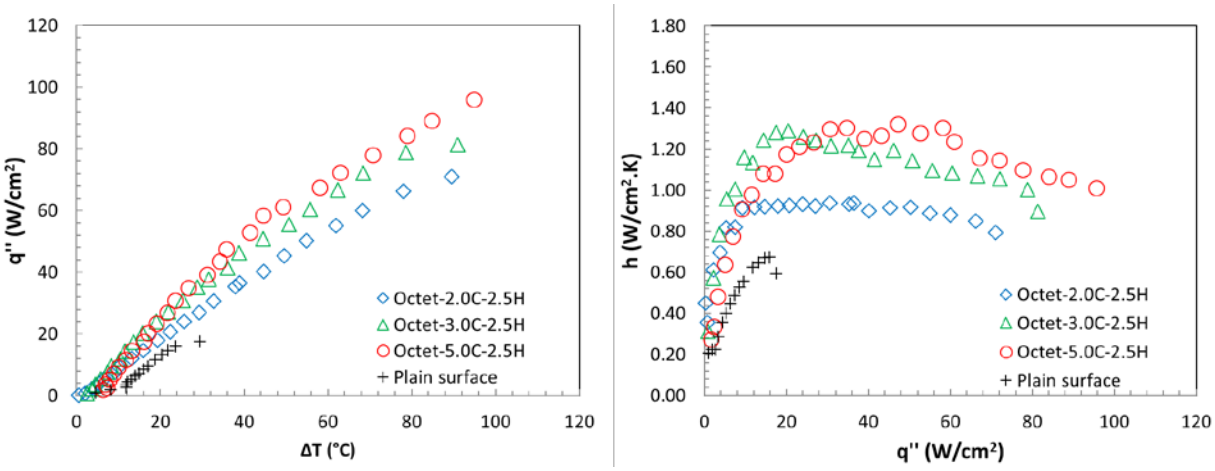

(a) (b)

Fig. 12. (a) Nucleate pool boiling curves and (b) heat transfer coefficients of different unit cell sizes at 2.5 mm height

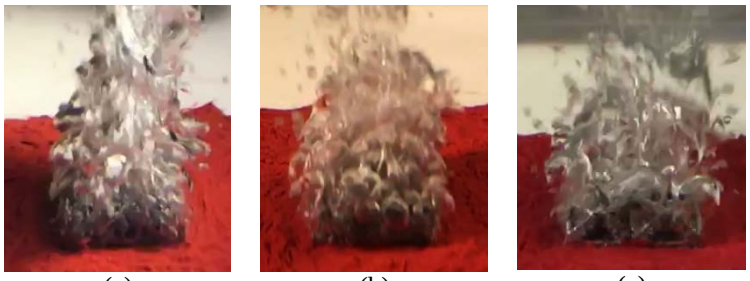

(a) (b) (c)

Fig. 13. Boiling patterns at heat flux of 40 W/cm^2 for (a) Octet-2.0C-2.5H (b) Octet-3.0C-2.5H and (c) Octet-5.0C-2.5H

Fig. 14(a) shows the pool boiling heat transfer performance of different unit cell sizes at fixed structure height of 5.0 mm. The 2-mm unit cell size performed the worst. A closer examination of Fig. 14(b) shows that Octet-3.0C-5.0H performed better than Octet-5.0C-5.0H in the range of 10-70 W/cm^2, above which there is a rapid deterioration of *h*. For Octet-3.0C-5.0H within this heat flux range, the combination of higher surface area, higher capillary-assisted liquid suction and sufficiently low bubble evacuation resistance allowed better nucleate boiling performance. However, above 70 W/cm^2, the high volume rate of bubble formation causes rapid coalescence and the dominant factor shifts to bubble evacuation resistance. Thus, the 5-mm unit cell size allowed sustained rapid bubble evacuation due to the larger pore size, and achieved the highest CHF at 107 W/cm^2.

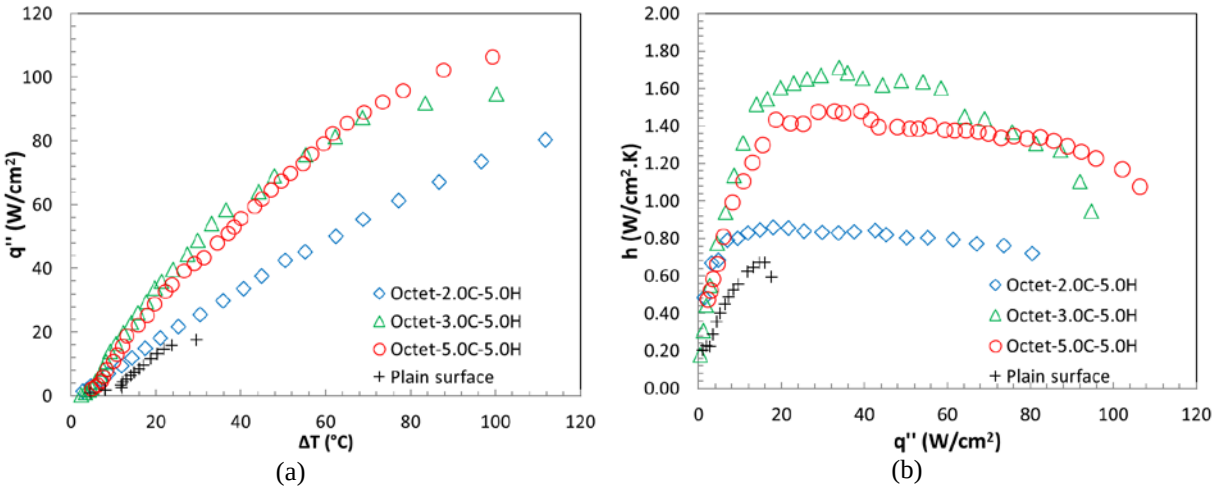

(a) (b)

DOI: 10.1016/j.ijheatmasstransfer.2017.12.148

Fig. 14. (a) Nucleate pool boiling curves and (b) heat transfer coefficients of different unit cell sizes at 5.0 mm height

Fig. 15(a) shows the pool boiling heat transfer performance of different unit cell sizes at fixed structure height of 10.0 mm. Once again, the 2-mm unit cell performed the worst. From Fig. 15(b), it is observed that Octet-5.0C-10.0H performed better than Octet-3.0C-10.0H for the entire range of heat flux. At the structure height of 10.0 mm, the dominant factor is bubble evacuation resistance as the bubbles need to traverse a greater height posed by the taller substrate. Thus, a larger pore diameter favors more rapid bubble evacuation and allows higher heat transfer rate. Fig. 16 shows the boiling patterns of the three substrates at heat flux of 40 W/cm^2. For the 2-mm and 3-mm unit cell sizes, high bubble evacuation resistance causes the bubbles to escape from the sides of substrates preferentially, leaving partial dry-out regions on the upper portion of the structures. However, bubbles could permeate the entire structure for the 5-mm unit cell size and sustain superior nucleate boiling.

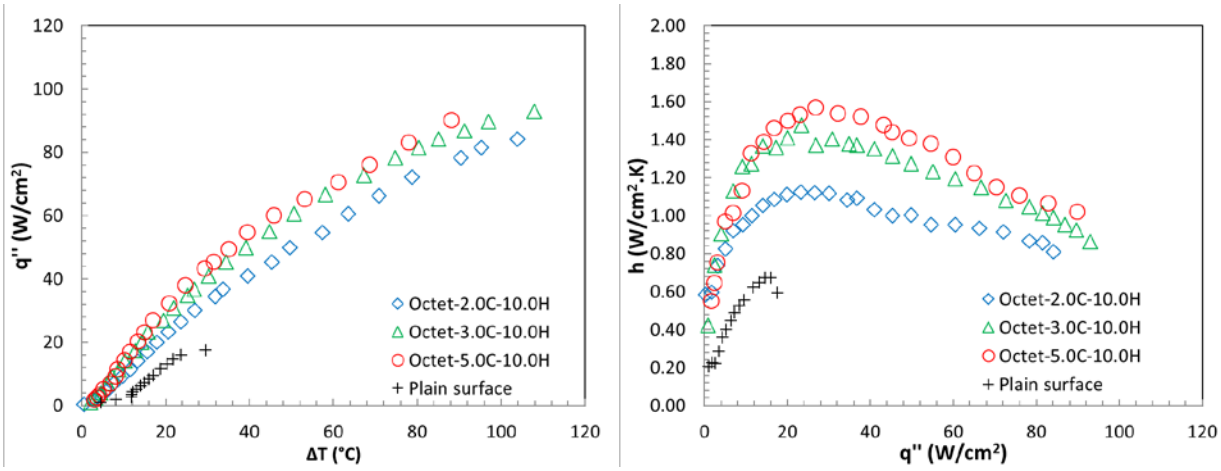

(a) (b)

Fig. 15. (a) Nucleate pool boiling curves and (b) heat transfer coefficients of different unit cell sizes at 10.0 mm height

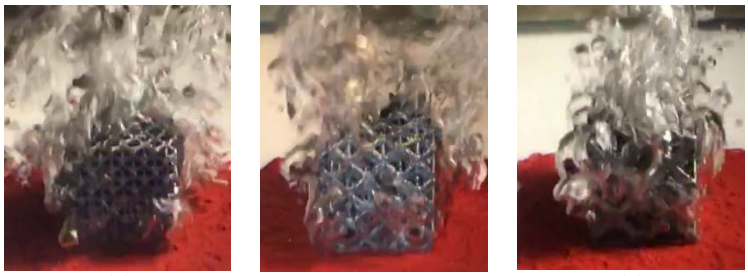

(a) (b) (c)

Fig. 16. Boiling pattern at heat flux of 40 W/cm^2 for (a) Octet-2.0C-10.0H (b) Octet-3.0C-10.0H and (c) Octet-5.0C-10.0H

4.3 Effect of height of structure

Fig. 17 shows the pool boiling heat transfer performance of different structure heights at fixed 2.0-mm unit cell size. The results show that Octet-2.0C-10.H performed the best, followed by Octet-2.0C-2.5H and Octet-2.0C-5.0H. The substrate of 2.5-mm height performed better than that of 5.0-mm height due likely to less bubble evacuation resistance. However, further increase of height to 10.0 mm allowed more surface area for nucleation, which surpassed the effect caused by higher bubble evacuation resistance. The boiling patterns are shown in Fig. 18. It can be observed that there are non-bubble regions for the 5-mm structure height which cause it to perform sub-optimally. Despite having some local non-bubble regions for the 10-mm structure height, the overall

DOI: 10.1016/j.ijheatmasstransfer.2017.12.148

nucleate boiling surface is significantly higher than the other two substrates, thus allowing more vigorous nucleation and leads to the highest nucleate boiling performance.

For the porous lattice substrates, a non-bubble region refers to a region where nucleation was observed not to have occurred periodically. These non-bubble regions typically occur for porous structures of small unit cell sizes and higher heights, where bubbles encountered more difficulty to evacuate from the structure. These non-bubble regions contributed to poorer heat transfer due to the lack of nucleation. However, the non-bubble region did not result in CHF because in that of plain surface, where a vapor film or permanent dry-out region occurred, intermittent liquid replenishment could occur for the porous structures. The non-bubble regions are marked by the blue circles in Fig. 18.

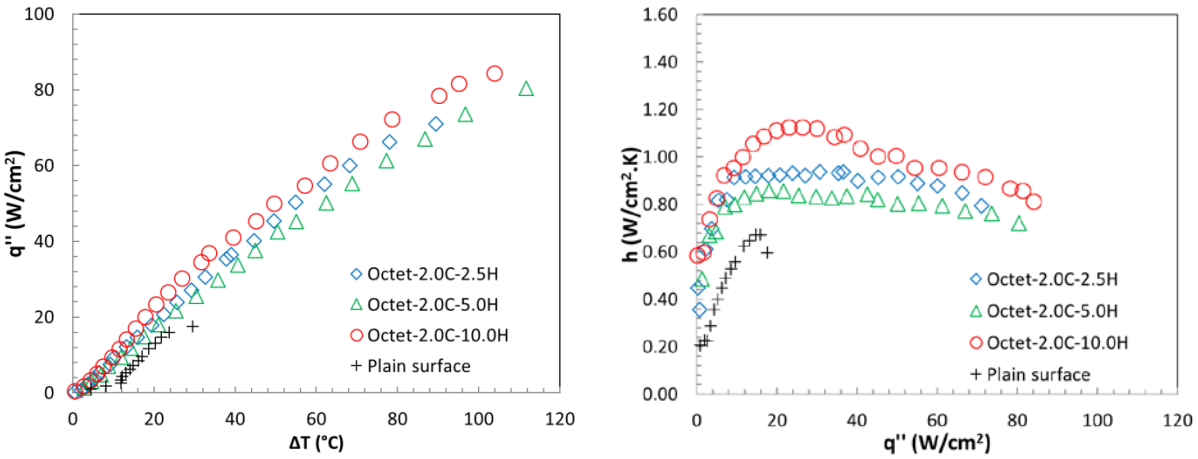

(a) (b)

Fig. 17. (a) Nucleate pool boiling curves and (b) heat transfer coefficients of different heights for 2-mm unit cell

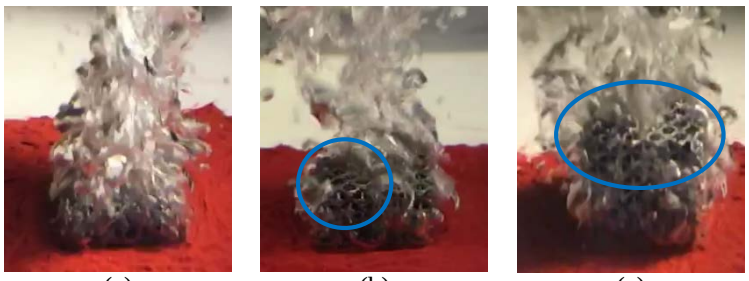

(a) (b) (c)

Fig. 18. Boiling patterns at heat flux of 40 W/cm^2 for (a) Octet-2.0C-2.5H (b) Octet-2.0C-5.0H and (c) Octet-2.0C-10.0H

Fig. 19(a) shows the pool boiling heat transfer performance of different structure heights at fixed 3.0-mm unit cell size. The substrate with 2.5-mm height performed worse than the 5.0 and 10.0-mm heights. The heat transfer performance increases with increasing height from 2.5 mm to 5.0 mm due likely to the larger surface area for nucleation. However, further increase of height to 10.0 mm resulted in a worse performance compared to the structure of 5.0 mm height, due likely to the additional bubble evacuation resistance imposed. From Fig. 19(b), it can be observed that the 5.0 mm height performed significantly better than the other two substrates above 15 W/cm^2. Thus, for the 3.0-mm unit cell size, a good balance of surface area and bubble evacuation resistance is achieved at the height of 5.0 mm.

DOI: 10.1016/j.ijheatmasstransfer.2017.12.148

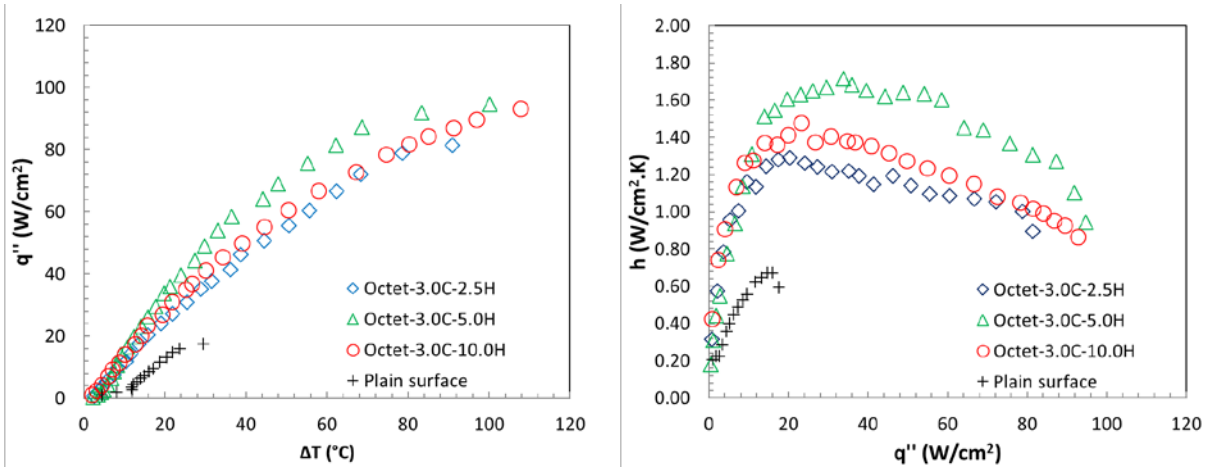

(a) (b)

Fig. 19. (a) Nucleate pool boiling curves and (b) heat transfer coefficients of different heights for 3-mm unit cell

Fig. 20(a) shows the pool boiling heat transfer performance of different structure heights at fixed 5-mm unit cell size. The substrate with 2.5-mm height performed worse than the 5.0 and 10.0-mm height. From Fig. 20(b), the 10.0-mm height structure performed better than the 5.0-mm height structure at heat flux below 50 W/cm^2, however the performance deteriorated to that of 2.5-mm height structure beyond 50 W/cm^2. The result shows that bubble resistance increases rapidly above 50 W/cm^2, which negates the effect of increased surface area for the 10.0-mm height structure. Thus, for the 5-mm unit cell size, a good balance of surface area and bubble evacuation resistance is achieved at the height of 5.0 mm.

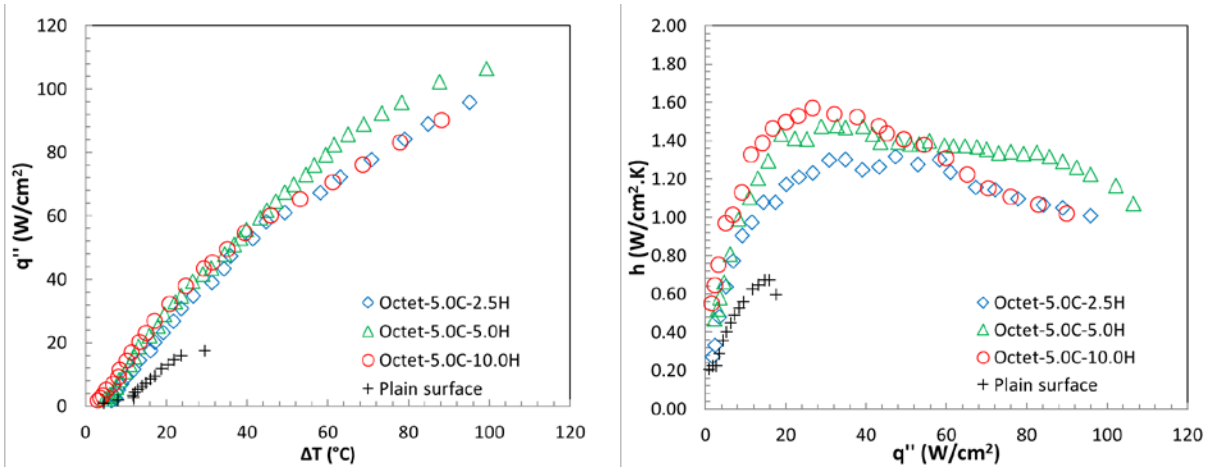

(a) (b)

Fig. 20. (a) Nucleate pool boiling curves and (b) heat transfer coefficients of different height for 5-mm unit cell

4.4 Summary of nucleate boiling performance and CHF

A summary of the nucleate pool boiling performances of all substrates is shown in Table 5. The enhancements of the average heat transfer coefficient and delay of CHF are benchmarked against both the plain surface and Octet-2.0C-5.0H structure. The nucleate boiling enhancement is attributed to the combined effects of increased surface area and capillary-assisted liquid suction but inhibited by form drag caused by bubble evacuation through the porous lattice structure. The competing effects are coupled together and the contributions of each factor are difficult to distinguish. For the same structure height, the smaller unit cell structure has a larger surface area and larger capillary-assisted liquid suction, albeit at the expense of larger bubble evacuation resistance. For the same unit cell size, a larger height favors a larger surface area for nucleation especially at higher heat fluxes but imposes a longer distance for bubbles to evacuate the structure Based on the results, the highest average heat transfer coefficient is achieved for Octet-3.0C-5.0H. Generally, the 2.0-mm unit cell size performed the worst. This shows that the bubble evacuation resistance plays a more dominant role as compared

DOI: 10.1016/j.ijheatmasstransfer.2017.12.148

to the surface area and capillary-assisted liquid suction, especially at high heat flux levels when the volumetric vapor generation rate is very high. The highest CHF is achieved by Octet-5.0C-5.0H at 107 W/cm^2. Generally, a higher CHF is achieved for larger unit cell sizes and intermediate structure height of 5.0 mm.

Table 5. Summary of nucleate pool boiling performances of all substrates

S/N	Name	h_{ave}	$\frac{h_{ave}}{h_{Plain}}$	$\frac{h_{ave}}{h_{Octet-2.0C-2.5H}}$	CHF	$\frac{CHF}{CHF_{Plain}}$	$\frac{CHF}{CHF_{Octet-2.0C-2.5H}}$
1	Plain surface	0.48	-	-	17.5	-	-
2	Octet-2.0C-2.5H	0.84	1.75	1.00	71	4.06	1.00
3	Octet-2.0C-5.0H	0.78	1.63	0.93	81	4.63	1.14
4	Octet-2.0C-10.0H	0.96	2.00	1.14	84	4.80	1.18
5	Octet-3.0C-2.5H	1.1	2.29	1.31	82	4.69	1.15
6	Octet-3.0C-5.0H	1.35	2.81	1.61	95	5.43	1.34
7	Octet-3.0C-10.0H	1.2	2.50	1.43	93	5.31	1.31
8	Octet-5.0C-2.5H	1.01	2.10	1.20	96	5.49	1.35
9	Octet-5.0C-5.0H	1.24	2.58	1.48	107	6.11	1.51
10	Octet-5.0C-10.0H	1.23	2.56	1.46	90	5.14	1.27

From the results, the use of increased structure height typically increases the heat transfer coefficient and CHF, though with the penalty of larger volume. The relative enhancements of *h* and CHF are computed with respect to the total volume of the substrate in Eqs. (8) and (9), respectively. For both cases, the relative enhancements are compared to reference values of the same unit cell size at 2.5-mm structure height. The results are summarized in Fig. 21. The relative enhancements are less than unity, which is likely due to the temperature drop along the structure at increased heights and its accompanied increased bubble evacuation resistance. It can also be observed that the relative enhancements decrease as the structure height is increased from 5.0 mm to 10.0 mm. Thus, if volume constraint is of high importance, a lower structure height is preferred.

$$\eta_h = \left(\frac{h_{ave}}{h_{ref}}\right) / \left(\frac{V}{V_{ref}}\right) \tag{8}$$

$$\eta_{CHF} = \left(\frac{h_{ave}}{h_{ref}}\right) / \left(\frac{V}{V_{ref}}\right) \tag{9}$$

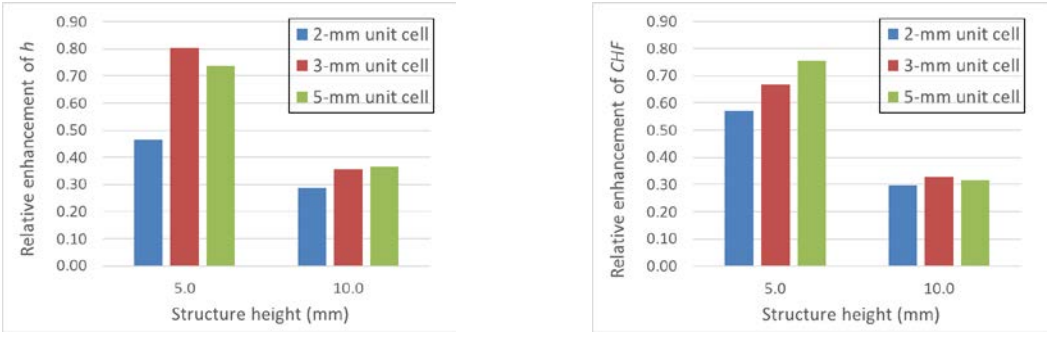

(a) (b)

Fig. 21. Relative enhancements of (a) heat transfer coefficient and (b) CHF with respect to volume

4.5 Comparison with results from the literature

DOI: 10.1016/j.ijheatmasstransfer.2017.12.148

The results of the current work are compared with those of other investigators using FC-72 as the working fluid as shown in Fig. 22(a). The comparison focuses on other surface modification techniques as there very few studies of pool boiling from porous foams with FC-72 as the working fluid. Compared to the current substrate of Octet-3.0C-5.0H, Rainey and You [7] obtained similar heat transfer performance with a finned surface of 2-mm height although the CHF was observed to occur at a lower heat flux of about 50 W/cm^2. Wu et al. [39] used TiO_2-coated nanoparticles on copper and achieved similar heat transfer performance but a low CHF of about 20 W/cm^2. Kim et al. [40] placed free particles of 0.6 to 0.8 μm on a plain copper surface which yielded significantly lower heat transfer performance. Sarangi et al. [41] deposited sintered copper particles of about 200 μm on a copper surface and obtained high heat transfer coefficients, but observed a lower CHF of about 10 W/cm^2 due to insufficient fluid replenishment. An et al. [42] used supersonically-sprayed reduced graphene oxide on a copper substrate which achieved moderate heat transfer performance and CHF of about 15 W/cm^2. Recently, Ho et al. [31] fabricated a micro-fin substrate of 400 μm height and achieved CHF of about 45 W/cm^2. As seen from the literature, surface modification techniques can enhance the heat transfer coefficients but were often limited in their capability to delay the CHF. The current designs of porous lattice structures thus have the potential to enhance the heat transfer coefficient and delay CHF effectively.

The comparison with published results of similar porous foam structures but with different fluids is shown in Fig. 22(b). Fluid properties play an important role in the heat transfer behavior and bubble dynamics for pool boiling. One of the more important properties is the latent heat of vaporization (h_{fg}). FC-72 has an h_{fg} value of 88 kJ/kg, while the values for acetone and water are 513 kJ/kg and 2257 kJ/kg, respectively. A higher h_{fg} allows a lower volumetric rate of bubble generation for the same heat removal which typically reduces coalescence and delays the CHF. Xu and Zhao [20] investigated the pool boiling from copper foams of 80 PPI porosity with water as the coolant and achieved high heat transfer coefficients and CHF of about 95 W/cm^2. Xu et al. [18] used copper foams of 30 PPI with acetone as the coolant and achieved higher heat transfer coefficients but a similar CHF of about 95 W/cm^2 as that of Octet-3.0C-5.0H. Ji et al. [43] used a 3D porous surface of about 2 mm thickness and acetone as the fluid, which achieved high CHF of 130 W/cm^2.

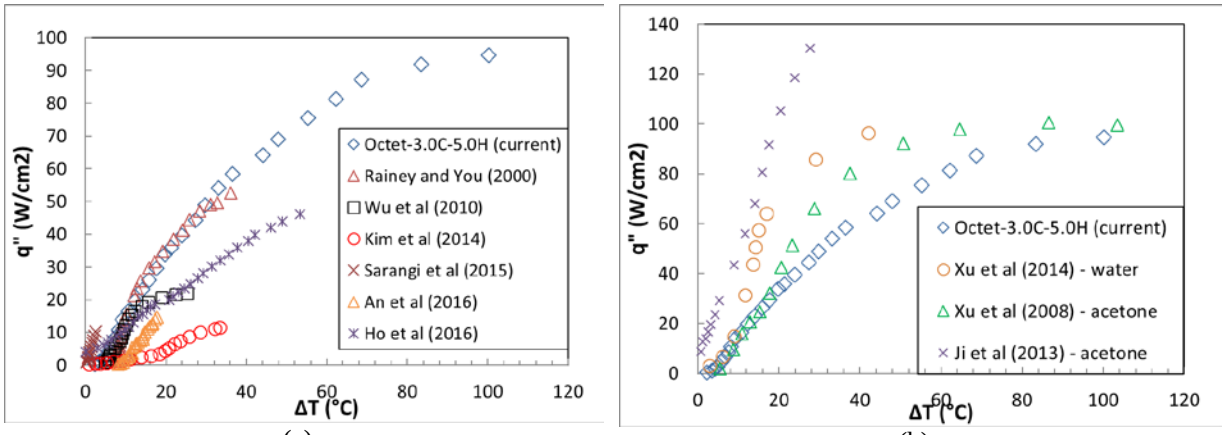

(a) (b)

Fig. 22. (a) Comparison with other investigators using FC-72 as the working fluid. (b) Comparison with porous foam or 3D porous materials using other fluids

5. Heat transfer mechanisms

In this section, the heat transfer mechanisms of the different heat flux levels in the nucleate boiling regime are proposed based on observations of the boiling process. In general, the porous structures allow better nucleation as compared to the plain surface due to the larger surface area and capillary-assisted liquid suction which allow better liquid replenishment. However, the solid struts of the porous structure impose form drag on the evacuating bubbles, causing bubble evacuation resistance. The bubble evacuation resistance due to form drag is elevated for higher heat flux, higher structure height and smaller unit cell size. The heat transfer mechanisms are classified under the low, mid, high and very-high heat flux levels. Due to the 3D geometry imposed by the

DOI: 10.1016/j.ijheatmasstransfer.2017.12.148

porous structures, there are numerous pathways for the liquid and vapor to flow. Depending on the type of structure, the boiling mechanism changes from stable to unstable form at high heat flux due to major liquid-vapor counter-flow.

5.1 Low heat flux level

In the low heat flux level, typically below 15 W/cm^2, nucleation generally occurs at the base of the porous structures. This is because the temperature is not high enough at the higher region of the porous structure to initiate nucleation. Bubbles generated are typically small and do not coalesce. The bubbles rise to the top of the porous structure by buoyancy and liquid replenishment can only occur from the sides of the structure, forming an orderly convection pathway, as shown in Fig. 23(a). In this heat flux level, there is minimal liquid-vapor counter-flow.

5.2 Mid heat flux level

In the mid heat flux level, typically between 15 and 40 W/cm^2, nucleation occurs readily throughout the porous structure as the temperature at the upper region of the structure becomes sufficiently high to activate the nucleation sites. The coalescence of bubbles can be readily observed. The bubbles typically coalesce within the porous structure and become bigger than the pore diameter before departure as shown in Fig. 23(b). This phenomenon was also observed by Xu et al. [18], and the term “cage-shaped” bubbles was used to describe it. The formation can be attributed to increased drag force of the bubbles within the porous structure and surface tension at the structure interface, thus delaying the bubble departure frequency.

Comparing to the plain surface, CHF occurs at 17.5 W/cm^2 due to hydrodynamic choking when the liquid cannot replenish effectively to the heated surface. However, due to increased surface area and capillary-assisted suction into the porous structure, nucleate boiling regime can be maintained. However, the formation of cage-shaped bubbles slightly impedes effective liquid replenishment causing some liquid-vapor counter-flow.

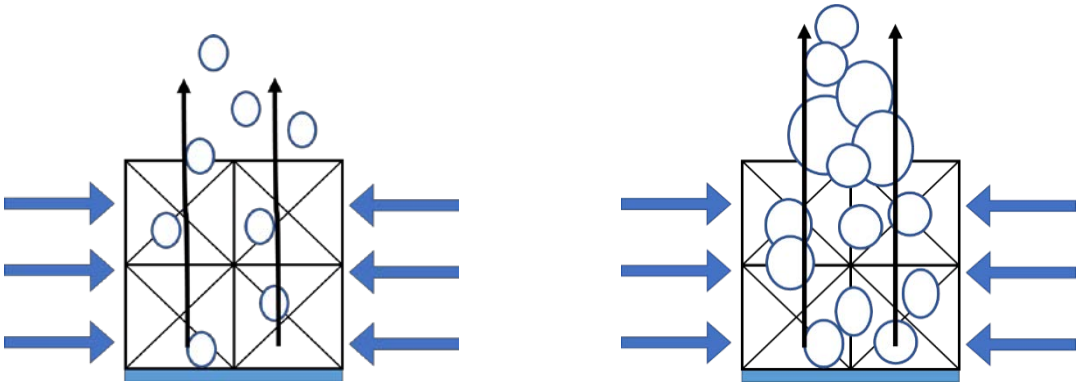

Fig. 23. Boiling mechanisms at (a) low heat flux level and (b) mid heat flux level

5.3 High heat flux level

The high heat flux level is typically between 40 and 80 W/cm^2. As the heat flux continues to increase, the temperature of the entire porous structure also increases and allows vigorous nucleation to take place throughout the entire structure. The high rate of bubble formation and increased drag force cause rapid coalescence within the porous structure and often lead to formation of mushroom-shaped bubbles encompassing the entire porous structure. At this juncture, two separate modes of stable and unstable patterns can be observed.

The stable boiling pattern is observed for porous structures of the larger pore diameter, i.e., 5-mm unit cell size. Due to the larger pore diameter, there is smaller drag force acting on the bubbles within the porous structure, allowing quicker evacuation of bubbles which occurs mainly from the top of the structure. This allows the

DOI: 10.1016/j.ijheatmasstransfer.2017.12.148

liquid-vapor counter-flow to be lowered as liquid replenishment can still readily occur from the sides, facilitating a good convection pathway as illustrated in Fig. 24(a).

However, for porous structures of smaller pore diameter, i.e., 2-mm and 3-mm unit cell sizes, an unstable boiling pattern is observed. The larger drag force caused by the smaller pore diameters, however, makes it difficult for the bubbles to evacuate upwards effectively through the porous structure, causing the bubbles to evacuate from the sides instead, as illustrated in Fig. 24(b). This causes a large liquid-vapor counter-flow as the orderly liquid replenishment is impeded, leading to a lower heat transfer coefficient and causing CHF to occur earlier than where the boiling pattern is stable.

Fig. 25 shows the experimental visualization of various porous structures with a height of 10.0 mm at heat flux of 70 W/cm^2. For Octet-2.0C-10.0H and Octet-3.0C-10.0H, vigorous nucleation occurs nearer to the base of the structures, whereas dry-spots were observed at the upper portion of the structure. This shows the unstable boiling process for such porous structures, which reduces the ability for fresh liquid to replenish to the base of the structure. However, it can be observed for Octet-5.0C-10.0H that bubbles can evacuate effectively through the upper portion of the structure. The fresh liquid can then replenish more effectively to the base, forming an orderly convection pathway, and thus, allowing a stable boiling process.

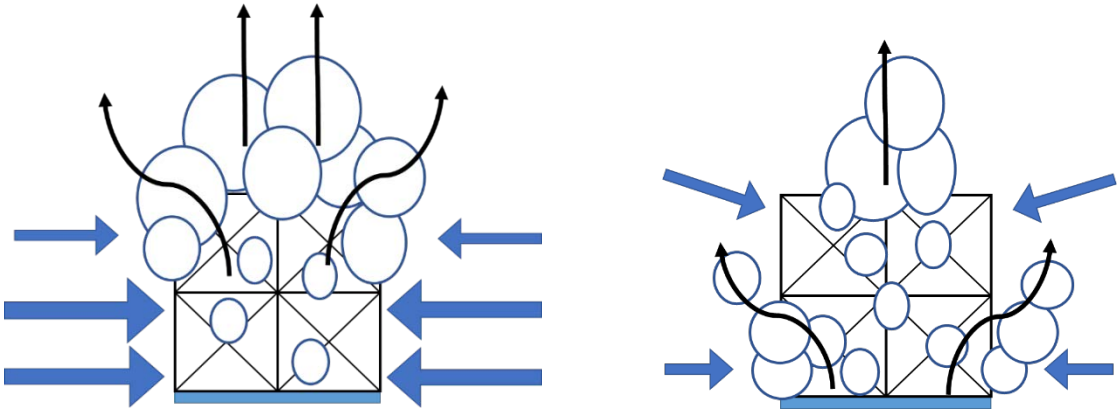

(a) (b)

Fig. 24. Boiling mechanism at high heat flux level for (a) stable boiling pattern and (b) unstable boiling pattern

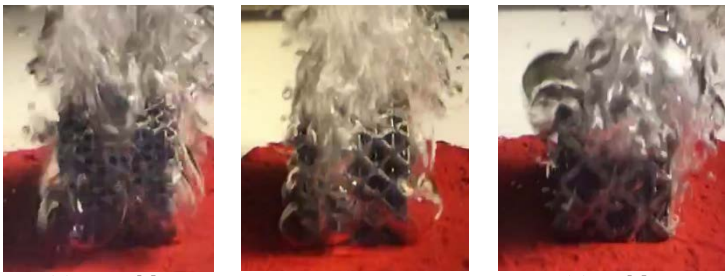

(a) unstable (b) unstable (c) stable

Fig. 25. Boiling patterns at heat flux of 70 W/cm^2 for (a) Octet-2.0C-10.0H (b) Octet-3.0C-10.0H and (c) Octet-5.0C-10.0H

5.4 Very high heat flux level

The very high heat flux level typically occurs above 80 W/cm^2. For the stable boiling pattern, further increase in heat flux causes higher rate of bubble formation. At this stage, an interesting phenomenon of bubble pulsation occurs. The different stages of the bubble pulsation are illustrated in Fig. 25 for the substrate of Octet-3.0C-2.5H at heat flux of 80 W/cm^2. Fig. 26(a) shows the departure of previous mushroom-shaped bubbles and the beginning of the suction stage. Fig. 26(b) shows the vaporization of liquid and formation of mushroom-shaped bubbles which encompass the entire substrate. Fig. 26(c) shows that the bubbles start to rise due to buoyancy. In

DOI: 10.1016/j.ijheatmasstransfer.2017.12.148

Fig. 26(d), necking is observed between the rising bubbles and substrate itself, and the cycle is completed in Fig. 26(e) when the bubbles depart, leaving behind a thin film surrounding the substrate. During the pulsation process, fresh liquid can replenish the porous structure during the period when the mushroom-shaped bubbles depart, thus allowing sustained nucleate boiling at very high heat flux and delaying the hydrodynamic choking effect which causes CHF. This phenomenon was also observed by Xu et al. [19] who reported that the pulsation frequency increased as the heat flux was increased. However, there is a limit to which the pulsation could keep up to replenish the fresh liquid at further increased heat flux, eventually causing CHF to be reached and an unstable increase in surface temperature.

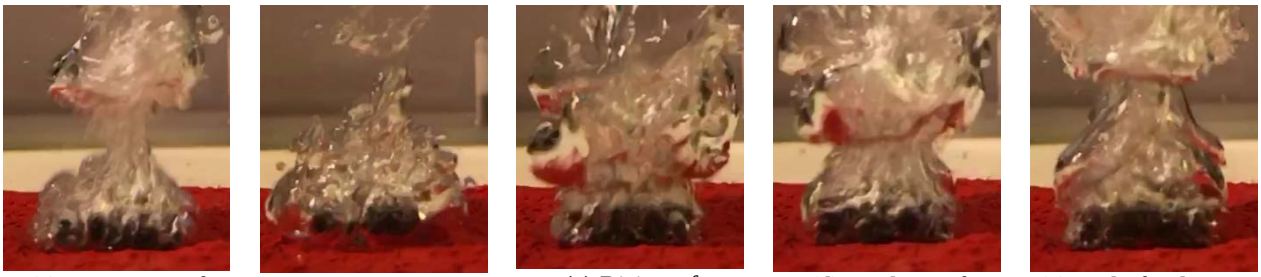

(a) Beginning of pulsation cycle (b) Vaporization stage (c) Rising of mushroom bubble (d) Necking of bubble (e) End of pulsation cycle

Fig. 26. Boiling patterns at heat flux of 80 W/cm^2 for Octet-3.0C-2.5H for different stages of pulsation

6. Conclusions

In this paper, pool boiling of porous structures was investigated with saturated FC-72 under atmospheric condition. Nine porous structures of the Octet-truss unit cell geometry were fabricated using the SLM technique. The porous structures were varied in terms of unit cell sizes of 2.0 mm, 3.0 mm and 5.0 mm, and structure heights of 2.5 mm, 5.0 mm and 10.0 mm. The authors are of the view that the substrates investigated in this paper can function as heat sinks for immersion cooling of electronic chips. The following conclusions are derived from this study:

1. The porous structure enhanced nucleate boiling heat transfer coefficient and delayed CHF effectively as compared to the plain surface as benchmark. The enhancement is attributed to the increased surface area, increased nucleation site density and capillary-assisted suction of the porous structure. The porous structure allows sustained liquid replenishment which delays the hydrodynamic choking and CHF significantly.

2. The effect of unit cell size is studied for the different substrates of the same structure height. The larger unit cell sizes of 3 mm and 5 mm are better for enhancing nucleate pool boiling as the dominant factor is bubble evacuation resistance, even though the smaller unit cell size of 2 mm has a larger surface area and capillary-assisted liquid suction. The best performing substrate is Octet-3.0C-5.0H and it has an average nucleate boiling heat transfer coefficient of 1.35 W/cm^2·K, which is 2.81 times that of the plain surface at 0.48 W/cm^2·K.

3. The effect of structure height is studied for the different substrates of the same unit cell size. A higher structure height has more surface area for nucleation although it imposes more bubble evacuation resistance. In general, the 5-mm height structure possesses a good balance between the two factors and allows higher nucleate boiling heat transfer coefficient. The highest CHF is achieved by Octet-5.0C-5.0H at 107 W/cm^2, which is 6.11 times that of the plain surface at 17.5 W/cm^2. The relative enhancements of heat transfer coefficient and CHF with respect to volume occupied by the porous structures were also tabulated. If volume constraint is of high importance, a lower structure height of 2.5-mm is more favorable for the application.

4. The heat transfer mechanisms are proposed for the different heat flux levels in the nucleate boiling regime of the porous structures based on visual observations. The boiling patterns are classified as low, mid, high and very-high heat flux levels. At low and mid heat flux levels, the boiling pattern change from discrete bubble departure to coalescence. At high heat flux level, two separate modes of stable and unstable boiling patterns are observed. For the stable boiling pattern, there are distinct bubble departure and liquid replenishment pathways

DOI: 10.1016/j.ijheatmasstransfer.2017.12.148

which facilitates good convection flow. However, for the unstable boiling pattern, there is major liquid-vapor counter-flow, which disrupts the orderly liquid replenishment pathway. At the very-high heat flux level, bubble pulsation is observed, which helps to sustain fresh liquid intake and high rate of vapor formation.

Acknowledgements

The authors would like to acknowledge the financial support for this project under Nanyang Technological University, Singapore's Academic Research Fund (AcRF) Tier 1 Grant No. RG 119/14. Funding of the SLM facilities by the National Research Foundation, Singapore is also gratefully acknowledged.

References

1. H. Honda, J.J. Wei, Enhanced boiling heat transfer from electronic components by use of surface microstructures. *Exp. Therm. Fluid Sci.* 28 (2004) 159-169.
2. M. Shojaeian, A. Koşar, Pool boiling and flow boiling on micro- and nanostructured surfaces. *Exp. Therm. Fluid Sci.* 63 (2015) 45-73.
3. D.E. Kim, D.I. Yu, D.W. Jerng, M.H. Kim, H.S. Ahn, Review of boiling heat transfer enhancement on micro/nanostructured surfaces. *Exp. Therm. Fluid Sci.* 66 (2015) 173-196.
4. K.C. Leong, J.Y. Ho, K.K. Wong, A critical review of pool and flow boiling heat transfer of dielectric fluids on enhanced surfaces. *Appl. Therm. Eng.* 112 (2017) 999-1019.
5. J.J. Wei, H. Honda, Effects of fin geometry on boiling heat transfer from silicon chips with micro-pin-fins immersed in FC-72. *Int. J. Heat Mass Transfer* 46 (2003) 4059-4070.
6. C.K. Yu, D.C. Lu, Pool boiling heat transfer on horizontal rectangular fin array in saturated FC-72. *Int. J. Heat Mass Transfer* 50 (2007) 3624-3637.
7. K.N. Rainey, S.M. You, Pool boiling heat transfer from plain and microporous, square pin-finned surfaces in saturated FC-72. *J. Heat Transfer* 122 (2000) 509-516.
8. P.S. O'Neill, C.F. Gottzmann, J.W. Terbot, *Novel heat exchanger increases cascade cycle efficiency for natural gas liquefaction*, in *Advances in Cryogenic Engineering* (1972) Springer US: Boston, MA. 420-437.
9. J.T. Cieśliński, Nucleate pool boiling on porous metallic coatings. *Exp. Therm. Fluid Sci.* 25(7) (2002) 557-564.
10. R. Webb, Nucleate boiling on porous coated surfaces. *Heat Transfer Eng.* 4 (1981) 71-82.
11. J.Y. Chang, S.M. You, Boiling heat transfer phenomena from microporous and porous surfaces in saturated FC-72. *Int. J. Heat Mass Transfer* 40 (1997) 4437-4447.
12. S.G. Liter, M. Kaviany, Pool-boiling CHF enhancement by modulated porous-layer coating: theory and experiment. *Int. J. Heat Mass Transfer* 44 (2001) 4287-4311.
13. C.M. Patil, S.G. Kandlikar, Pool boiling enhancement through microporous coatings selectively electrodeposited on fin tops of open microchannels. *Int. J. Heat Mass Transfer* 79 (2014) 816-828.
14. J.Y. Ho, K.C. Leong, C. Yang, Saturated pool boiling from carbon nanotube coated surfaces at different orientations. *Int. J. Heat Mass Transfer* 79 (2014) 893-904.
15. C.Y. Zhao, Review on thermal transport in high porosity cellular metal foams with open cells. *Int. J. Heat Mass Transfer* 55 (2012) 3618-3632.
16. J. Paek, B. Kang, S. Kim, J. Hyun, Effective thermal conductivity and permeability of aluminum foam materials. *Int. J. Thermophys.* 21 (2000) 453-464.
17. K.C. Leong, H.Y. Li, Theoretical study of the effective thermal conductivity of graphite foam based on a unit cell model. *Int. J. Heat Mass Transfer* 54 (2011) 5491-5496.
18. J. Xu, X. Ji, W. Zhang, and G. Liu, Pool boiling heat transfer of ultra-light copper foam with open cells. *Int. J. Multiphase Flow* 34 (2008) 1008-1022.
19. Z.G. Xu, Z.G. Qu, C.Y. Zhao, W.Q. Tao, Experimental correlation for pool boiling heat transfer on metallic foam surface and bubble cluster growth behavior on grooved array foam surface. *Int. J. Heat Mass Transfer* 77 (2014) 1169-1182.
20. Z.G. Xu, C.Y. Zhao, Pool boiling heat transfer of open-celled metal foams with V-shaped grooves for high pore densities. *Exp. Therm. Fluid Sci.* 52 (2014) 128-138.

DOI: 10.1016/j.ijheatmasstransfer.2017.12.148

21. Z.G. Xu, C.Y. Zhao, Experimental study on pool boiling heat transfer in gradient metal foams. *Int. J. Heat Mass Transfer* 85 (2015) 824-829.
22. L.W. Jin, K.C. Leong, I. Pranoto, Saturated pool boiling heat transfer from highly conductive graphite foams. *Appl. Therm. Eng.* 31 (2011) 2685-2693.
23. I. Pranoto, K.C. Leong, L.W. Jin, The role of graphite foam pore structure on saturated pool boiling enhancement. *Appl. Therm. Eng.* 42 (2015) 163-172.
24. C.K. Chua, K.F. Leong, *3D Printing and Additive Manufacturing: Principles and Applications (with Companion Media Pack) of Rapid Prototyping*. 2014, World Scientific Publishing Co Inc.
25. N. Read, W. Wang, K. Essa, M.M. Attallah, Selective laser melting of AlSi10Mg alloy: Process optimisation and mechanical properties development. *Materials & Design* (1980-2015) 65 (2015) 417-424.
26. M. Wong, I. Owen, C.J. Sutcliffe, A. Puri, Convective heat transfer and pressure losses across novel heat sinks fabricated by Selective Laser Melting. *Int. J. Heat Mass Transfer* 52 (2009) 281-288.
27. K.K. Wong, J.Y. Ho, K.C. Leong, T.N. Wong, Fabrication of heat sinks by Selective Laser Melting for convective heat transfer applications. *Virtual Phys. Prototyp.* 11 (2016) 159-165.
28. J.Y. Ho, K.K. Wong, K.C. Leong, T.N. Wong, Convective heat transfer performance of airfoil heat sinks fabricated by selective laser melting. *Int. J. Therm. Sci.* 114 (2017) 213-228.
29. R. Neugebauer, B. Müller, M. Gebauer, T. Töppel, Additive manufacturing boosts efficiency of heat transfer components. *Assembly Automation* 31 (2011) 344-347.
30. J.Y. Ho, K.C. Leong, Cylindrical porous inserts for enhancing the thermal and hydraulic performance of water-cooled cold plates. *Appl. Therm. Eng.* 121 (2017) 863-878.
31. J.Y. Ho, K.K. Wong, K.C. Leong, Saturated pool boiling of FC-72 from enhanced surfaces produced by Selective Laser Melting. *Int. J. Heat Mass Transfer* 99 (2016) 107-121.
32. J. Esarte, J.M. Blanco, A. Bernardini, J.T. San-José, Optimizing the design of a two-phase cooling system loop heat pipe: Wick manufacturing with the 3D selective laser melting printing technique and prototype testing. *Appl. Therm. Eng.* 111 (2017) 407-419.
33. S.L. Sing, L.P. Lam, D.Q. Zhang, Z.H. Liu, C.K. Chua, Interfacial characterization of SLM parts in multi-material processing: Intermetallic phase formation between AlSi10Mg and C18400 copper alloy. *Materials Characterization* 107 (2015) 220-227.
34. V.S. Deshpande, N.A. Fleck, M.F. Ashby, Effective properties of the octet-truss lattice material. *J. Mech. Phys. Solids* 49 (2001) 1747-1769.
35. X. Ji, J. Xu, H. Li, G. Huang, Switchable heat transfer mechanisms of nucleation and convection by wettability match of evaporator and condenser for heat pipes: Nano-structured surface effect. *Nano Energy* 38 (2017) 313-325.
36. 3M, *Fluorinert Electronic Liquid FC-72 Product Information*. 2009.
37. J.R. Taylor, *An Introduction to Error Analysis*, second ed. 1997, Sausalito, California: University Science Books.
38. N. Zuber, *Hydrodynamic Aspects of Boiling Heat Transfer*, Ph.D. thesis, University of California, Los Angeles, 1959. (Also available as AECU-4439 Physics and Mathematics.)
39. W. Wu, H. Bostanci, L.C. Chow, Y. Hong, M. Su, J.P. Kizito, Nucleate boiling heat transfer enhancement for water and FC-72 on titanium oxide and silicon oxide surfaces. *Int. J. Heat Mass Transfer* 53 (2010) 1773-1777.
40. T.Y. Kim, J.A. Weibel, S.V. Garimella, A free-particles-based technique for boiling heat transfer enhancement in a wetting liquid. *Int. J. Heat Mass Transfer* 71 (2014) 808-817.
41. S. Sarangi, J.A. Weibel, S.V. Garimella, Effect of particle size on surface-coating enhancement of pool boiling heat transfer. *Int. J. Heat Mass Transfer* 81 (2015) 103-113.
42. S. An, D.-Y. Kim, J.-G. Lee, H.S. Jo, M.-w. Kim, S.S. Al-Deyab, J. Choi, S.S. Yoon, Supersonically sprayed reduced graphene oxide film to enhance critical heat flux in pool boiling. *Int. J. Heat Mass Transfer* 98 (2016) 124-130.
43. X. Ji, J. Xu, Z. Zhao, W. Yang, Pool boiling heat transfer on uniform and non-uniform porous coating surfaces. *Exp. Therm. Fluid Sci.* 48 (2013) 198-212.